

Article

Satellites HY-1C and Landsat 8 Combined to Observe the Influence of Bridge on Sea Surface Temperature and Suspended Sediment Concentration in Hangzhou Bay, China

Shuyi Huang ¹, Jianqiang Liu ² , Lina Cai ^{1,*}, Minrui Zhou ¹, Juan Bu ¹ and Jieni Xu ¹

¹ Marine Science and Technology College, Zhejiang Ocean University, Zhoushan 316004, China; ehuangshuyi@163.com (S.H.); 15156255226@163.com (M.Z.); 16621727803@163.com (J.B.); xujieni922@163.com (J.X.)

² National Satellite Ocean Application Service (NSOAS), Beijing 100081, China; jqliu@mail.nsoas.org.cn

* Correspondence: cknown@zjou.edu.cn

Received: 8 August 2020; Accepted: 13 September 2020; Published: 17 September 2020



Abstract: We analyzed the influence of a cross-sea bridge on the sea surface temperature (SST) and suspended sediment concentration (SSC) of Hangzhou Bay based on landsat8_TIRS data and HY-1C data using an improved single window algorithm to retrieve the SST and an empirical formula to retrieve the SSC. In total, 375 paired sampling points and 70 transects were taken to compare the SST upstream and downstream of the bridge, and nine transects were taken to compare the SSC. The results show the following. (i) In summer, when the current flows through the bridge pier, the downstream SST of the bridge decreases significantly, with a range of 3.5%; in winter, generally, the downstream SST decreases but does not change as obviously as in summer. The downstream SSC increases obviously. (ii) The range of influence of the bridge pier on the downstream SST is about 0.3–4.0 km in width from the bridge and that on the downstream SSC is approximately 0.3–6.0 km. (iii) When the current flows around the pier, a portion of the flow is dispersed in upward and downward directions; the downward flow generates local scour. When the scouring at the front end of the pier stops, the upward flow behind the pier brings the sediment and the bottom cold water downstream, causing the downstream SST to decrease and the SSC to increase. (iv) The other portion passes around the pier, which generates a wake vortex. Once a wake vortex is released, a low-pressure center appears, sucking the sediment and the bottom cold water to the downstream sea surface, reducing the downstream SST and raising the SSC. (v) The range of reduction of the SST downstream of the bridge is shorter than the range of increase in the SSC. This is because the wake vortices have an effect in the 0.3–4.0 km downstream but not in the 4.0–6.0 km. Therefore, the SST and SSC are affected within the range of 0.3–4.0 km by wake vortices, while in the 4.0–6.0 km region, the SSC is still high due to the transport of sediment by currents.

Keywords: HY-1C; landsat 8; SST; SSC; Hangzhou Bay Bridge

1. Introduction

In recent years, more and more cross-sea bridges, such as Hangzhou Bay Bridge, Hong Kong–Zhuhai–Macao Bridge and Jiaozhou Bay Bridge, have been built. A cross-sea bridge is an important transportation junction connecting various cities and economic zones. However, the construction and operation of a cross-sea bridge also has an impact on the marine environment, including the hydrodynamic environment [1,2], sediment [3,4] and sea surface temperature (SST) [5,6].

The marine hydrodynamic environment plays a vital role in material transport and energy transfer. The construction of cross-sea bridge causes the hydrodynamics to change, and there have been many studies focusing on it in recent years. The tidal current numerical model [7–9] was established, and it was found that the piers had an influence on tide, tidal current and residual current. Furthermore, prior researchers calculated the current velocity of the water area near Jiaozhou Bay Bridge by the analogical principle of simulation. The variation of the flow velocity was relatively greater at only ten meters upstream and downstream, and the water flow field was not affected by the presence of bridge piers beyond 180 m upstream and 110 m downstream [7–9]. The numerical simulation of the tidal dynamic change at Qingdao Jiaozhou Bay Bridge was performed using an unstructured finite volume ocean model—FVCOM [1], and prior researchers discovered that when the tide was rising and ebbing, the flow velocity increased between two adjacent sets of piers, while the flow velocity decreased around the piers. Based on MIKE 21 Flow Modules by Danish Hydraulic Institute (DHI), Zhao et al. [2] found that the different water levels on both sides of the cross-sea bridge can induce a barotropic current, increasing the flow velocity north of the bridge and decreasing the southern flow velocity.

Sediments are the main living places and food sources of benthic organisms and play a significant role in the marine ecological environment [3]. The construction of a cross-sea bridge changes the suspended sediment concentration (SSC). The influence of East Sea Bridge on sediment transport based on Medium Resolution Imaging Spectrometer (MERIS) and Thematic Mapper (TM) satellite images was studied [4], and it was revealed that the SSC increased near the axis of bridge, while it decreased in the area 5 km away from the sand belt. Comparing to historical data, prior studies found that during the construction of the cross-sea bridge in Jiaozhou Bay [2], the sediments on the north side of the bridge become coarser and those on the south side become finer; this was mainly because the increased flow on the north side of the bridge brought coarser seabed sediments. Meanwhile, researchers observed that the downstream SSC increased at 3.0–6.5 km away from the bridge when the upstream SSC was low in Hangzhou Bay. However, when the upstream SSC was greater than 400 mg/L, the SSC decreased downstream [10]. In recent years, scholars who have combined satellite observation with SSC inversion have established a large number of models [11–13]. We applied the latest HY-1C data to retrieve the SSC in the study area [11].

Since the construction of a cross-sea bridge has an effect on many ocean environmental factors, whether it will change the SST is also a subject worthy of study. We have consulted a lot of references at home and abroad, but none of them is about the influence of cross-sea bridges on sea surface temperatures, and we always want to know the influence and mechanism of such on sea surface temperatures caused by cross-sea bridges, which is why we perform this research.

The SST is a significant parameter of material and energy exchange between the air and sea. Therefore, it was applied for studying meteorological changes, fish growth laws and typhoon movement paths. The SST is also related to the changes in and succession of ecosystems as well as the wind [5], Kuroshio [6], monsoons, El Nino and global warming. Air temperature and wind speed affected the SST by changing the turbulent heat flux, which was based on the correlation between SST anomalies and turbulent heat flux [14]. The discovery that the SST of the Yellow Sea and the East China Sea increased year by year in the winter of fifty-eight years [15] indicates that the SST of the seas was related to the oscillation of the North Pacific Ocean. Meanwhile, the Coriolis Stokes force [16] had an effect on the depth of the mixed layer and the SST by acting on the upper ocean.

SST inversion algorithms includes a single-channel algorithm and multi-channel split window algorithm [17–19]. Jiménez-Muñoz and Sobrino [17] put forward a generalized single-channel algorithm, which only applied atmospheric moisture content and effective channel wavelength to calculate the SST, and the same parameters and equations could be applied to different thermal sensors. The Qin single-channel algorithm [18], based on the surface heat radiation conduction equation, applied surface emissivity, atmospheric transmittance and average atmospheric temperature to perform surface-temperature inversion. Furthermore, an improved mono-window algorithm [19],

based on the Qin single-channel algorithm, was used for the temperature inversion from Landsat 8 data. Considering the influence of atmospheric water content and the zenith angle of the sensor perspective, McConaghy [20] derived the SST inversion empirical formula for National Oceanic and Atmospheric Administration (NOAA) channel 5 based on the atmospheric radiation transfer equation, which established the relationship between the remote-sensing brightness temperature and surface temperature.

The hydrodynamic environment makes an obvious difference to the SSC and SST in coastal waters. The SSC is very high in coastal waters, especially in Hangzhou Bay, with high turbidity. The waters with high turbidity, such as the middle of Hangzhou Bay, the west of the bay, the northeast of the bay near the Yangtze River Estuary and the shallow water sandbanks in the south of the bay, have large SSCs [11,13]. The monitoring of SST is of great significance to the study of the hydrodynamic environment. When the SST of a certain water area decreases, it may be the effect of upwelling [21] or a vortex street. The pier of a cross-sea bridge can change the surrounding hydrodynamic environment; one is local scour, and the other is wake vortices around the pier [22]. When the scour in front of the pier stops, the upstream flow behind the pier brings sediment and bottom cold water downstream, resulting in a decrease in the downstream SST and an increase in the downstream SSC [23]. The wake vortices absorb the sediment and bottom cold water to the downstream sea surface, reducing the downstream SST and increasing the downstream SSC. According to the decreasing range of the SST, the action range of wake vortices can be deduced. For the study of the local marine environment, these two are the key indicators. Therefore, this paper wants to reveal the influence of the construction of the cross-sea bridge on two aspects of the surrounding water environment. It lays a foundation for further research on the influence of the bridge on other marine environmental factors.

In this paper, to study the effect of the bridge on both of the SST and SSC, we retrieved the SST using the improved mono-window algorithm proposed by Wang et al. [19], from the Landsat 8_TIRS sensor data. And the SSC was retrieved from HY-1C data using an empirical formula posed by Cai et al. [11].

The structure of this article is as follows. Section 2 is an introduction to the data and methods. Section 3 describes the currents in the study area and the retrieved SST and SSC distributions using the improved mono-window algorithm model and the empirical formula. Sections 4 and 5 are the discussion and conclusion.

2. Data and Methods

2.1. Study Area

Hangzhou Bay is located in the Yangtze river delta area, adjacent to the east China sea and Zhoushan Islands (Figure 1). The bay is like a funnel in shape. The top of the bay, from Jiaxing to Shaoxing, is about 20 km. The mouth of the bay is about 100 km, ranging from the Luchaogang in Shanghai to Zhenhai District in Ningbo. The water area is about 4800 square kilometers. From the top to Zhapu, the seabed slopes down gently, forming a huge sand bar; from Zhapu to the mouth, the topography is flat. Hangzhou Bay is the estuary of the Qiantang River and the Yangtze River. The two rivers transport a large amount of sediment and fresh water into the Hangzhou Bay [24]. The average annual sediment transport of the Yangtze River is 3.90×10^8 tons, and that of the Qiantang River is 2.50×10^6 tons [25]. Hangzhou Bay is a macro-tidal estuary, and the tidal variation in the bay is the semidiurnal tide. The mean tidal range is 4–6 m at the top of the bay and at the mouth of the bay is 3–4 m [26]. The hydrodynamic environment of the bay is complex. In the north of Hangzhou Bay, the rising tide is strong, while in the south, it is weak [27]. The residual current is roughly close to the north shore of the bay, and the average velocity is around 0.2 m/s [28]. In summer, the SST in the west is higher than that in the east, while in winter, it is the opposite. Hangzhou Bay Bridge (HBB), spanning the channel of the bay, starts from Jiaxing and ends at Ningbo. It is the longest cross-sea bridge in the world, 36 km long, including 32 km at sea, with a huge number of works and a total of 1428 piers [13].



Figure 1. The map of the Hangzhou Bay and the location of Hangzhou Bay Bridge (HBB). The red star is the measuring point.

2.2. Remote-Sensing Data

2.2.1. Landsat 8 Data

The Landsat 8 was successfully launched from California in the United States in 2013. It is a sun-synchronous near-polar satellite with an altitude of 705 km and an inclination of 98.2°, with an orbital regression period of 98.9 min. The satellite is equipped with two sensors, Operational Land Imager (OLI) and Thermal Infrared Sensor (TIRS). It is the first Landsat series satellite with two thermal infrared channels. OLI has nine bands with a high spatial resolution of 30 m for band1, band2, band3, band4, band5, band6, band7 and band9 and 15 m for band8. It has the following improvements over Enhanced Thematic Mapper (ETM+) sensor: new coastal and cirrus bands have been added, the wavelength range of the near-infrared band has been adjusted to exclude the influence of water vapor absorption at 0.825 μm , and the Narrow Panchromatic band is easy to distinguish between vegetation and non-vegetation. The TIRS have two thermal infrared bands with a spatial resolution of 100 m. The setting of the Landsat 8 parameters is shown in Table 1. Information about the images is shown in Table 2.

Table 1. Information about Landsat 8.

Sensor	Band	Wavelength (μm)	Spatial Resolution (m)
OLI	Band1-COASTAL	0.433–0.453	30
	Band2-Blue	0.450–0.515	30
	Band3-Green	0.525–0.600	30
	Band4-Red	0.630–0.680	30
	Band5-NIR	0.845–0.885	30
	Band6-SWIR1	1.560–1.660	30
	Band7-SWIR2	2.100–2.300	30
	Band8-PAN	0.500–0.680	15
	Band9-Cirrus	1.360–1.390	30

Table 1. Cont.

Sensor	Band	Wavelength (μm)	Spatial Resolution (m)
TIRS	Band10-TIR	10.60–11.19	100
	Band11-TIR	11.50–12.51	100

Table 2. Remote-sensing data.

Number	Band	Acquired Date
1	Band10-TIR	12 July 2013
2	Band10-TIR	29 August 2013
3	Band10-TIR	3 December 2013
4	Band10-TIR	13 June 2014
5	Band10-TIR	4 November 2014
6	Band10-TIR	22 December 2014
7	Band10-TIR	26 January 2016
8	Band10-TIR	15 January 2018
9	Band10-TIR	17 December 2018
10	Band10-TIR	18 January 2019

2.2.2. HY-1C Data

The Chinese HY-1C satellite was launched from the Taiyuan Satellite Launch Center in 2018, carrying five payloads including Chinese Ocean Color and Temperature Scanner (COCTS), Coastal Zone Imagery (CZI), Ultraviolet Imagery (UV), Satellite Calibration Spectrometer (SCS) and Automatic Identification System (AIS). With a spatial resolution of 50 m, CZI has a blue band, green band, red band and near infrared band. Compared with the HY-1A and HY-1B satellites, the observation accuracy and the range of HY-1C are greatly improved. In this paper, four of the CZI images from HY-1C were analyzed. The parameters of the CZI sensor and information about the images are shown in Table 3.

Table 3. The parameters of the Coastal Zone Imagery (CZI) sensor and information about the images.

Band	Wavelength (μm)	Spatial Resolution (m)	Date
Band1-Blue	0.421–0.500	50	11 November 2019
Band2-Green	0.517–0.598	50	14 November 2019
Band3-Red	0.608–0.690	50	18 February 2020
Band4-NIR	0.761–0.891	50	21 February 2020

2.3. In Situ Data

The SCL9-2 direct-reading ammeter was used to measure the tidal current in the study area from 29 February to 2 March, from 6 to 7 March and from 10 to 11 March in 2012. The measuring point is marked in Figure 1 (Table 3). The in situ data were measured by us.

SCL9-2, suitable for rivers, lakes, estuaries and shallow seas with water depths less than 80 m, is mainly composed of an underwater detector, water display and transmission cable, and a three-core, light, weight-bearing cable which is used to connect the underwater detector and the water monitor [29]. In the underwater detector, the velocity sensor is composed of a propeller and magnetic sensor. Under the impact of water flow, the spinning speed is proportional to the measured velocity. The actual flow rate can be measured by the internal calibration of the instrument [30].

After the preparation of the instrument was completed, the underwater detector was placed at a predetermined depth, the normal measurement mode was chosen, the starting value of the calendar clock was set, the flow direction value and flow rate value on the water display were read and, finally, the data were exported.

2.4. Data Processing

In this paper, fifteen Landsat 8 images were analyzed, and ten without clouds were selected as examples, shown in Table 2. Firstly, ENVI5.1 was used for the radiometric calibration of the remote-sensing images, converting the pixel gray values to radiance intensity values. In order to eliminate the effects of atmospheric gases on the surface reflection, a fast line-of-sight atmospheric analysis of spectral hypercubes (FLAASH) [31], an atmospheric correction module based on the radiative transfer calculation method of MODTRAN4, was applied for correcting the image. Finally, the improved Mono-Window Algorithm inverted the SST of Hangzhou Bay using band4, band5 and band10. Band4 is the fourth band of Landsat 8, and it is the red band with a wavelength of 0.630–0.680 μm ; band5 is the near infrared band with a wavelength of 0.845–0.885 μm ; and band10 is the thermal infrared band with a wavelength of 10.60–11.19 μm . The information is shown in Table 1.

In order to carry out the inversion of the SST with the improved Mono-Window Algorithm, we made some preparations. First, the normalized difference vegetation index (*NDVI*) was calculated so that the Vegetation Proportion (P_V) could be obtained. Then, the P_V was utilized to obtain the land surface emissivity (ε_λ); we usually take the ε_λ of a water body as 0.991 for band10. Finally, the ε_λ was introduced into the Equations (4)–(6) to invert the land surface temperature. At this point, since the land surface emissivity was taken as 0.991 for band10, we obtained the SST.

2.4.1. Normalized Difference Vegetation Index (*NDVI*) Calculation

The *NDVI* can reflect the distribution of vegetation [32]. For *NDVI* values larger than 0.5, the pixel is considered as fully vegetation. When the *NDVI* values are between 0 and 0.2, the pixel is considered as bare soil [33]. The calculation formula for the *NDVI* is:

$$NDVI = \frac{NIR - R}{NIR + R} \quad (1)$$

where *NIR* is near infrared band of Landsat 8, and *R* is the red band of Landsat 8. *NIR* (band5 for Landsat 8) represents the near infrared band reflectance, and *R* (band4 for Landsat 8) represents the red band reflectance without units [32].

2.4.2. Vegetation Proportion Calculation

The $NDVI^{THM}$, which was first introduced by Sobrino [33], was applied to distinguish between soil pixels ($NDVI < NDVI_s$) and pixels of full vegetation ($NDVI > NDVI_v$). The vegetation proportion represents the percentage of vegetation area in the total area, and it can be calculated from the *NDVI* [34]. The formula is:

$$P_V = \left(\frac{NDVI - NDVI_s}{NDVI_s - NDVI_v} \right)^2 \quad (2)$$

where P_V is the Vegetation Proportion, $NDVI_v$ is the *NDVI* for a fully vegetated pixel and $NDVI_s$ is the *NDVI* for a fully soil pixel. The $NDVI_v$ and $NDVI_s$ values can be extracted from the *NDVI* histogram. Values of $NDVI_v = 0.5$ and $NDVI_s = 0.2$ were proposed to apply in global conditions [35].

2.4.3. Land Surface Emissivity Estimation

The land surface emissivity represents the ratio of surface radiation to blackbody radiation at the same temperature and wavelength, which can reflect the intensity of the surface radiation. It can be calculated using Equation (3) [34].

$$\varepsilon_\lambda = \begin{cases} \varepsilon_{s\lambda}, & NDVI < NDVI_s \\ \varepsilon_{s\lambda} + (\varepsilon_{v\lambda} - \varepsilon_{s\lambda})P_V, & NDVI_s \leq NDVI \leq NDVI_v \\ \varepsilon_{v\lambda}, & NDVI > NDVI_v \end{cases} \quad (3)$$

where ε_λ is the land surface emissivity, and $\varepsilon_{s\lambda}$ and $\varepsilon_{v\lambda}$, are, respectively, the soil and vegetation emissivity. The surface consists of vegetation, towns and water. The variation of the suspended sediment concentration has little effect on the sea surface emissivity [36], so for sea water with uniform physical and chemical characteristics, ε_λ can be taken as an approximate value. In this paper, the specific emissivity of the sea surface was 0.991 [19,37].

2.4.4. An Improved Mono-Window Algorithm

Qin's mono-window algorithm is proposed for TM images, and it is not suitable for Landsat 8 images [18]. Fei Wang et al. [19] improved the algorithm and made it applicable to Landsat 8 images. The improved mono-window algorithm is shown as:

$$T_S = [a_{10}(1 - C_{10} - D_{10}) + (b_{10}(1 - C_{10} - D_{10}) + C_{10} + D_{10})T_{10} - D_{10}T_a]/C_{10} \quad (4)$$

$$C_{10} = \varepsilon_{10} \times \tau_{10} \quad (5)$$

$$D_{10} = (1 - \tau_{10}) \times [1 + (1 - \varepsilon_{10}) \times \tau_{10}] \quad (6)$$

where T_S is the land surface temperature, ε_{10} is the land surface emissivity (the value assigned was 0.991) and τ_{10} is the atmospheric transmittance, which can be found on NASA's website (<http://atmcorr.gsfc.nasa.gov/>) [38]. T_a is the effective mean atmospheric temperature, and T_{10} is the brightness temperature, where $a_{10} = -62.7182$, $b_{10} = 0.4339$.

The linear relationship between the effective mean atmospheric temperature (T_a) and the near-surface air temperature (T_0) under different conditions was provided [18]. In mid-latitude summer, $T_a = 16.0110 + 0.9262T_0$; in mid-latitude winter, $T_a = 19.2704 + 0.9112T_0$.

For the brightness temperature (T_{10}), it is derived from the thermal spectral radiance through the approximation of the Plank radiance function:

$$R_{10} = M_{10}Q_{10} + A_{10} - O_{10} \quad (7)$$

$$T_{10} = \frac{K_2}{\ln\left(1 + \frac{K_1}{R_{10}}\right)} \quad (8)$$

where R_{10} is the thermal spectral radiance, and Q_{10} is the digital number (DN) value of band10. M_{10} , A_{10} , O_{10} , K_1 and K_2 are the band-specific thermal conversion constants for band10. $M_{10} = 0.0003342$, $A_{10} = 0.1$, $K_1 = 774.89$ ($W \times m^2 \times sr^{-1} \times \mu m^{-1}$), and $K_2 = 1321.08$ (K). Additionally, $O_{10} = 0.29$ ($W \times m^2 \times sr^{-1} \times \mu m^{-1}$) before 3 February 2014; after that, it should not be considered.

2.4.5. SSC Retrieval

Firstly, the polynomial geometric correction model [39] was used for geometric correction to eliminate the geometric distortion in the satellite images. Then, radiometric calibration and atmospheric correction were carried out. The digital number (DN) is the brightness value of remote-sensing image pixel, recording the gray value of ground object. Radiometric calibration can convert the DN value of a satellite image into reflectivity according to a radiometric calibration formula. The atmospheric correction based on the 6SV radiative transfer model [40] and MODIS aerosol data [41] was to eliminate the influence of Rayleigh scattering and aerosol scattering. The atmospheric correction algorithm was applied for HY-1C CZI in turbid waters to obtain the remote-sensing reflectance. At last, the SSC of Hangzhou Bay was retrieved by the red band and near infrared band based on an empirical formula [11], which was applied for HY-1C. The calculation is as follows:

$$SSC = 64.54 - 7033.83 \times R_{RED} + 96027 \times R_{NIR} \quad (9)$$

where SSC is the suspended sediment concentration (mg/L), and R_{RED} and R_{NIR} are the remote-sensing reflectance of the third (RED) and fourth (NIR) bands after atmospheric correction. The calculations were performed in Python 3.7.

Sampling was performed upstream and downstream of the bridge. In the Landsat 8 images, the upstream sampling points were 0.5 km away from the bridge and the downstream sampling points were 1.5 km away from the bridge. A total of 125 paired points were sampled in summer, 125 paired points were sampled in autumn, and 125 paired points were sampled in winter. Then, for each image, three transects on both sides of the bridge were analyzed for temperature. The first transect is 0.5 km upstream of the bridge, the second is 0.5 km downstream, and the third is 1.5 km downstream. Finally, four transects were taken for each image to observe the changes in the downstream SST. In the HY-1C data, nine transects were taken to obtain the influenced range.

3. Result

3.1. Tidal Current

The data in Figure 2 are from the in situ data in Table 4. The tide type of Hangzhou Bay is an irregular semidiurnal tide. In a lunar day, there are two high tides and two low tides. In a day, the highest tide level can reach 24.5 m (Figure 2b), the corresponding lowest tide level is 20.6 m, and the average tidal range is 3.9 m. The two adjacent high tides have the phenomenon of diurnal inequality during the rising and ebbing tides. The rising tide time is shorter than the ebbing tide time.

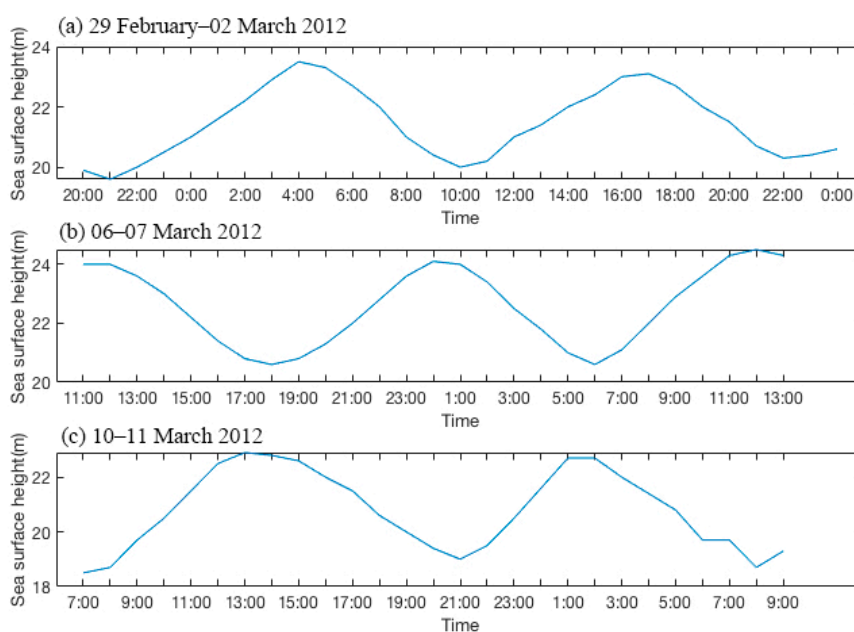


Figure 2. Tidal levels for 29 February–2 March 2012 (a), 6–7 March 2012 (b) and 10–11 March 2012 (c).

Table 4. In situ data.

Number	Location	Time	Measurements Taken
1	30.35° N, 122.13° E	29 February–2 March 2012	Depth
2	30.35° N, 122.13° E	6–7 March 2012	Velocity and direction of flow
3	30.35° N, 122.13° E	10–11 March 2012	flow

The data in Figure 3 are from the in situ data in Table 4. The sizes of the arrows represent the velocities of the flows, and the directions of the arrows represent the directions. The angle calculation method takes north as zero degrees and increases clockwise: 90° for east, 180° for south and 270° for

west. The positive direction of the Y axis represents east. It can be seen from Figure 3 that the tidal current in Hangzhou Bay is characterized by an irregular semidiurnal tide, which is a reciprocating flow from east to west. The velocity varies with time, and the regular variation is similar to the tide level. The maximum velocity is in the process of the rising tide and ebbing tide, and the minimum velocity is at high tide and low tide. In a day, the maximum velocity is 1.69 m/s and the minimum velocity is 0.28 m/s at the average depth during the rising tide; in the ebbing tide, the maximum velocity is 1.92 m/s and the minimum velocity is 0.18 m/s at the average depth (Figure 3(c1)), but the overall rising tide velocity is similar to the ebbing tide velocity. The surface current velocity is generally larger than the average current velocity, and the maximum is 2.01 m/s at high tide and 2.10 m/s at low tide (Figure 3(c2)).

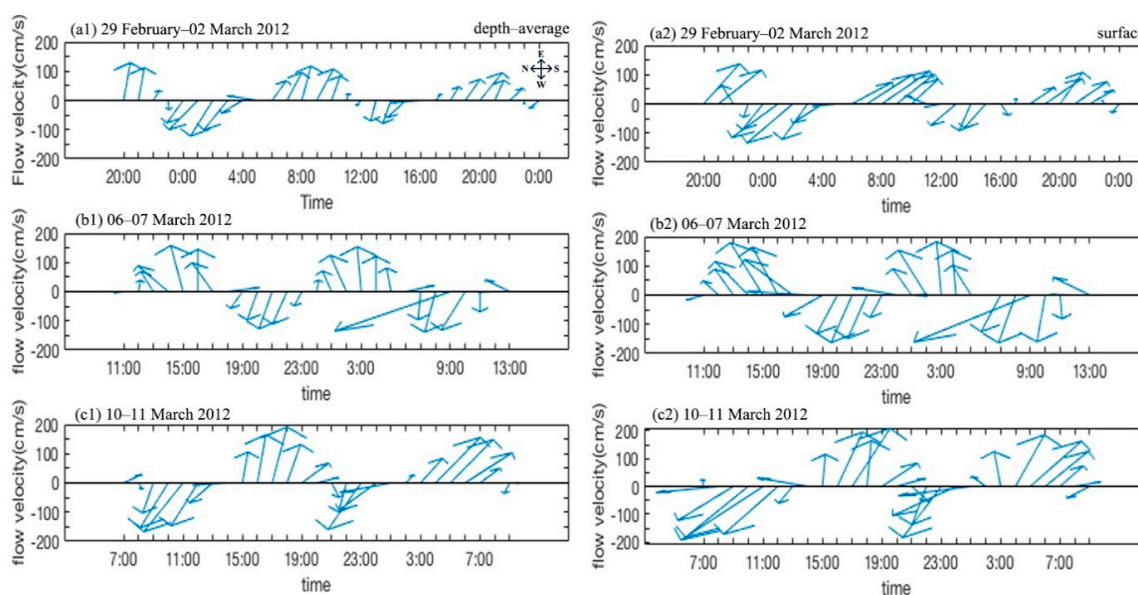


Figure 3. Flow's velocity and direction at average depth for 29 February–2 March 2012 (a1), 6–7 March 2012 (b1) and 10–11 March 2012 (c1). Flow's velocity and direction on the surface for 29 February–2 March 2012 (a2), 6–7 March 2012 (b2) and 10–11 March 2012 (c2).

The data in Figure 3 are to show that the tidal current characteristics of Hangzhou Bay are irregular semidiurnal tides, which are stable. The current direction is an east–west reciprocating flow. The current velocity changes with time with a sinusoidal function shape, which is similar every day. Therefore, this rule can be explained by the data measured at any time. It is the same reason for studying the influence of a cross-sea bridge on its surrounding marine environment. The tidal current characteristics of Hangzhou Bay are an essential condition for studying the influence of the pier on the SST and SSC. The east–west direction of the tidal current will interact with the pier and produce a wake vortex downstream of the pier.

3.2. SST of Hangzhou Bay

The sea surface temperature of Hangzhou Bay changes seasonally (Figure 4). In summer, the SST is higher in the west than the east, and the temperature gradually decreases from the inside to the outside of the bay. In winter, the SST is lower in the west than the east, and the temperature gradually increases from the inside to the outside of the bay. At the mouth of Hangzhou Bay, the SST of the south and the north is evenly distributed in summer (Figure 4c,d), while in winter, the SST of the south is higher than the north at the same longitude (Figure 4a,b,e,f,i,j). In the middle of the bay, the temperature in the north of bay is lower than that in the south during the rising and ebbing tides in summer (Figure 4c,d). In winter, it is higher in the north than the south (Figure 4a,b,e,f,i,j). The temperature difference between the north and south is about 1.5–2 °C. In the Qiantang River

estuary at the top of Hangzhou Bay and the northeast part of Hangzhou Bay near the Yangtze River Estuary, the SST is higher in summer than in the surrounding waters, but it is lower in winter. From the local map of Hangzhou Bay, it can be seen that there is a section of water area downstream of the bridge, whose sea surface temperature is relatively low (marked in Figure 4), which is lower than the SST upstream and in other waters downstream (Figure 4(a1)–(e1)).

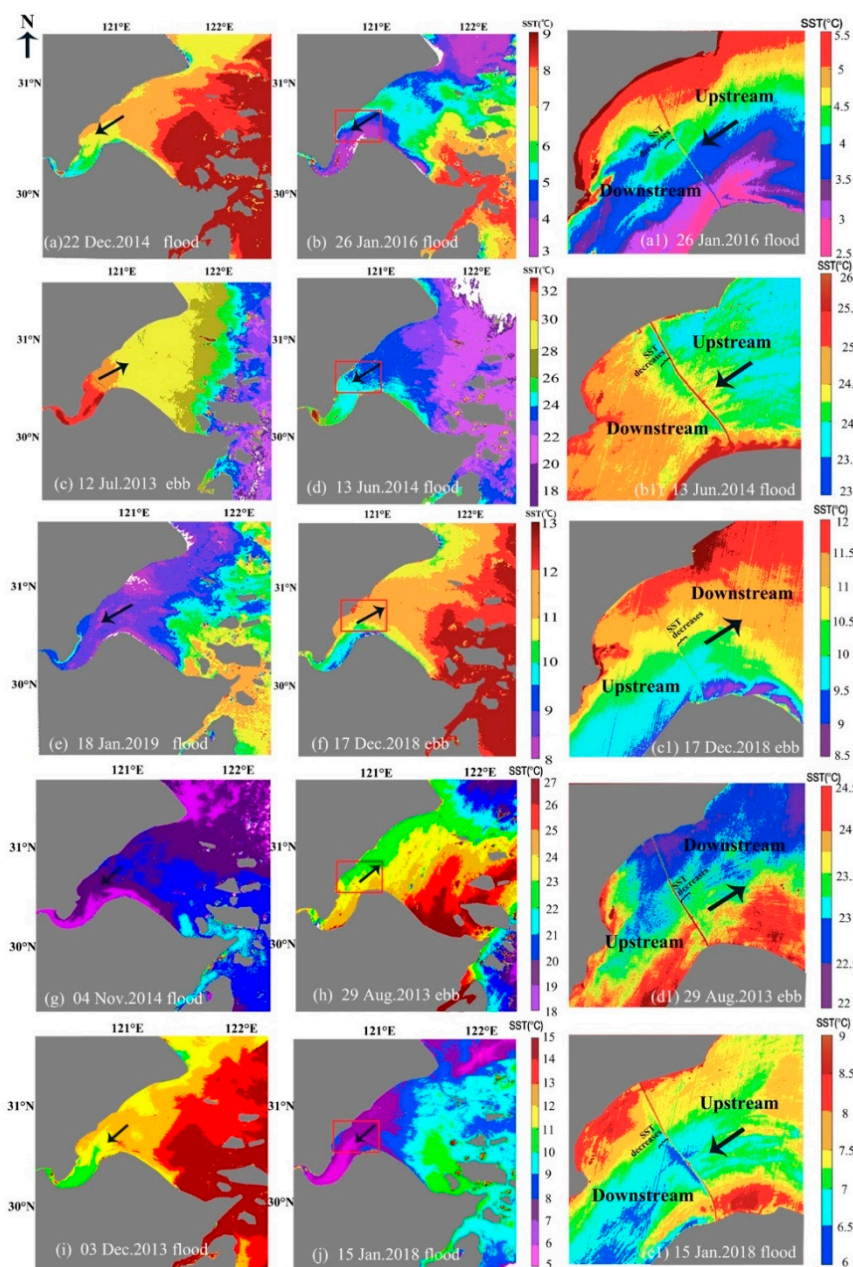


Figure 4. Sea surface temperatures retrieved from Landsat 8 images on 22 December 2014 (a), 26 January 2016 (b), 12 July 2013 (c), 13 June 2014 (d), 18 January 2019 (e), 17 December 2018 (f), 4 November 2014 (g), 29 August 2013 (h), 3 December 2013 (i) and 15 January 2018 (j). (a,b,d,e,g,i,j) flood; (c,f,h) ebb. (a1,b1,c1,d1,e1) Sea surface temperature (SST) distribution near the Hangzhou Bay bridge. The red box shows the waters near the Hangzhou Bay Bridge.

3.3. Decreased SST Downstream of the Bridges

There are two bridges, Hangzhou Bay Bridge and East Sea Bridge. Hangzhou Bay Bridge is 36.0 km long, and East Sea Bridge is 32.5 km. We focus on the Hangzhou Bay Bridge, which is longer than East Sea Bridge. The direction of the bridge facing the water flow is defined as upstream, and the other side is downstream. In this paper, points upstream and downstream of the bridge were sampled in summer, autumn and winter. Along the current, a pair of matching points were taken simultaneously upstream and downstream of the bridge. The upstream sampling points were 0.5 km away from the bridge, and the downstream sampling points were 1.5 km away from the bridge. A total of 125 paired points were sampled in summer, 125 paired points were sampled in autumn, and 125 paired points were sampled in winter. In summer, the SST of the upstream and downstream sampling points was 22.0–25.0 °C; in autumn, the SST was 18.8–22.2 °C, and in winter, the SST was 6.0–7.4 °C. The results show that in these three seasons, the SSTs upstream and downstream are positively correlated (Figure 5d,f,h), and the upstream SST is generally higher than the downstream SST. In summer, when the current flows through the bridge piers, the downstream SST declines significantly (Figure 5c). In autumn and winter, after the current flows through the bridge piers, the SST of the most downstream sampling points reduces, but the SST at about 25.2% of the sampling points increases (Figure 5e,g). Although the change in SST is not obvious, in general, the downstream SST decreases. The change in SST in summer is −3.5–1.0%; in autumn, it is −2.0–1.0%, and in winter, it is −10.0–3.0%. The size of the change downstream in summer and autumn is relatively concentrated, and the size in winter is great.

Three transects were taken on both sides of the bridge. The first transect was 0.5 km upstream of the bridge, the second was 0.5 km downstream, and the third was 1.5 km downstream. It can be seen that in summer and winter, when the tide rises and ebbs, the SST upstream is generally higher than that downstream. In summer, the upstream SST is significantly higher than that downstream (Figure 6a,b). In winter, the upstream SST is higher than the downstream SST at high tide, while an obvious change in the downstream SST cannot be seen at low tide in winter, but the upstream SST is higher than the downstream SST by calculation. In winter, the SST upstream and downstream decreased from the northwest to southeast of the bridge (Figure 6c,d). It is evident from Figure 6 that the temperature difference between the upstream and downstream areas in summer is larger than that in winter. The average temperature difference between 0.5 km upstream and 0.5 km downstream is 0.18 °C in summer and 0.13 °C in winter, while the average temperature difference between 0.5 km upstream and 1.5 km downstream is 0.33 °C in summer and 0.20 °C in winter.

A transect was taken perpendicular to the bridge, and the SST upstream and downstream were measured along the transect to compare changes in the SST on both sides of the bridge. It was found that when the current flows through the bridge piers, the downstream SST drops significantly within the range of 0.3–4.0 km in summer (Figure 7a,b). Outside the 4.0 km range, the downstream SST is higher than the upstream SST during the rising tides (Figure 7b); the upstream SST is always higher than the downstream SST during the ebbing tides (Figure 7a). In winter, the downstream SST also decreases within the range of 0.3–4.0 km during high and low tide (Figure 7c,d). It can be seen from Figure 7 that downstream, within the distance of 0.3–4.0 km from the bridge, the SST is lower than both the upstream SST and the SSTs of other downstream waters. Therefore, this distance is the range of SST decreases. In summer, the SST decreased by 0.12–0.60 °C, while in winter, the SST decreased by 0.12–0.60 °C. In general, the SST reduces in the range of 0.12–0.6 °C.

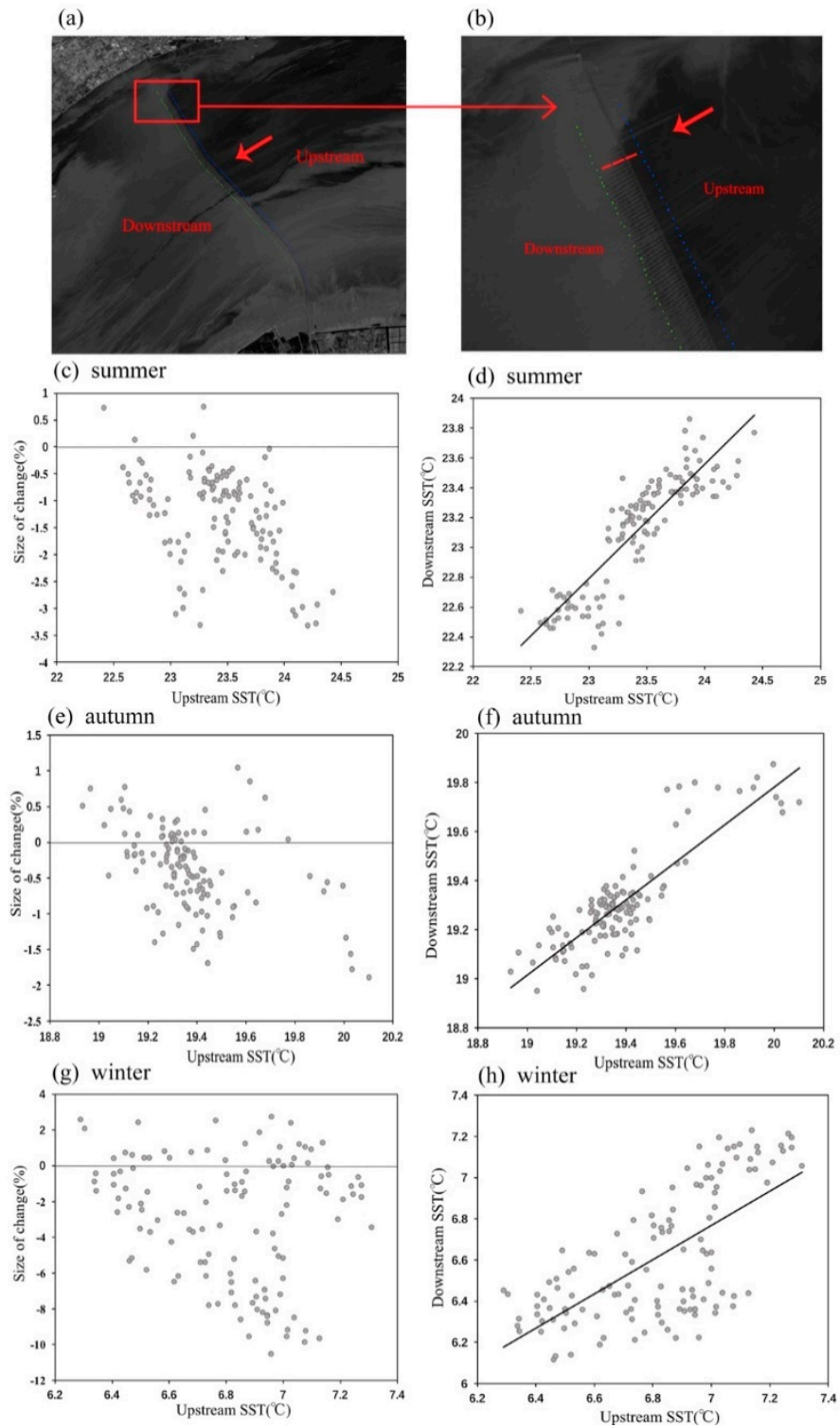


Figure 5. (a,b) Distribution of sampling points. (c,e,g) Regression analysis between upstream SST and change in SST downstream during rising and ebbing tides. Formula is $(\text{upstream SST} - \text{downstream SST}) / (\text{upstream SST}) \times 100\%$. Positive values denote SST increases, and negative values denote SST decreases. (d,f,h) Regression analysis of upstream and downstream SSTs during rising and ebbing tides.

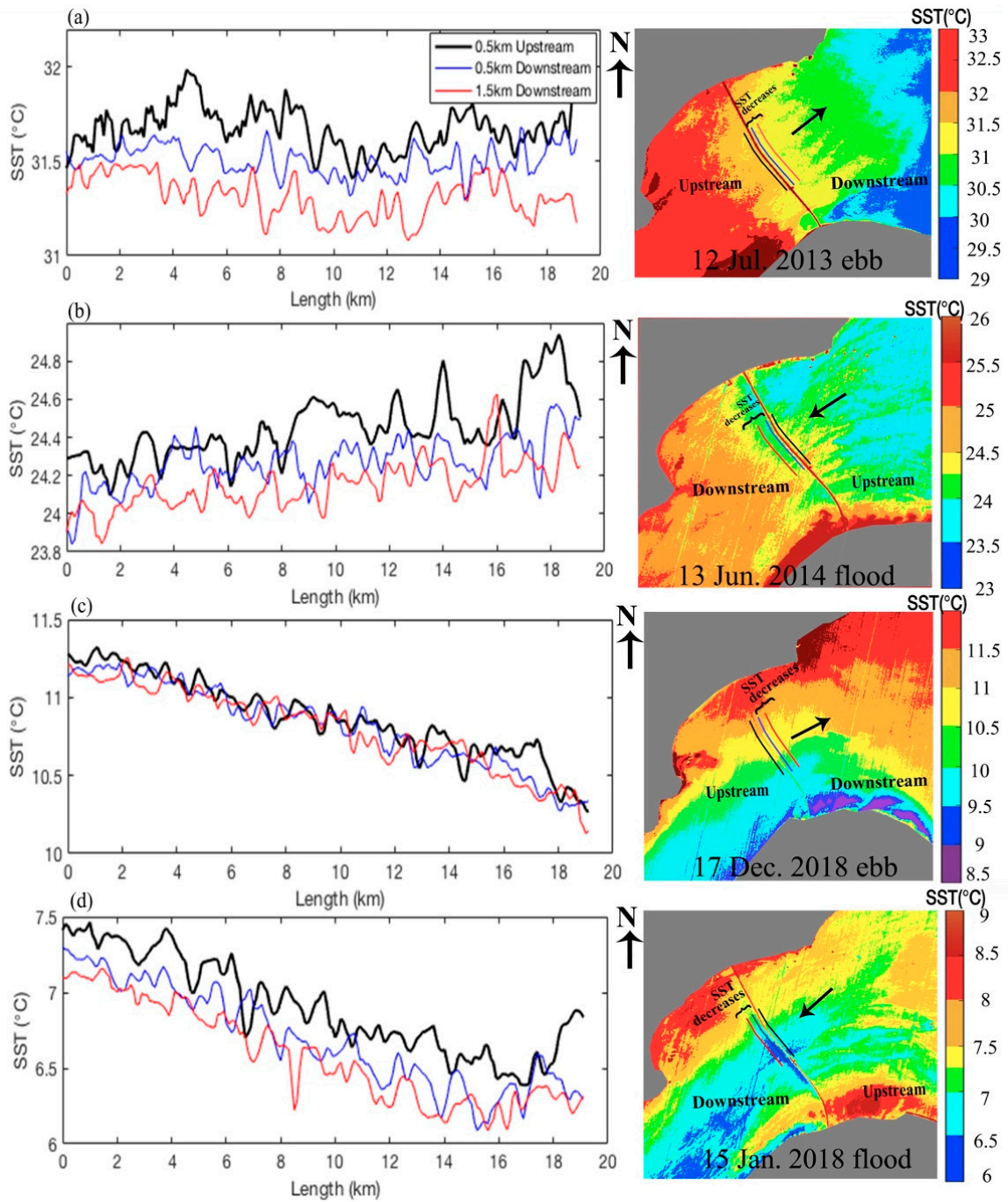


Figure 6. Upstream SST and downstream SST on 12 July 2013 (a), 13 June 2014 (b), 17 December 2018 (c) and 15 January 2018 (d). Black line is 0.5 km upstream of the bridge, blue line is 0.5 km downstream, and red line is 1.5 km downstream.

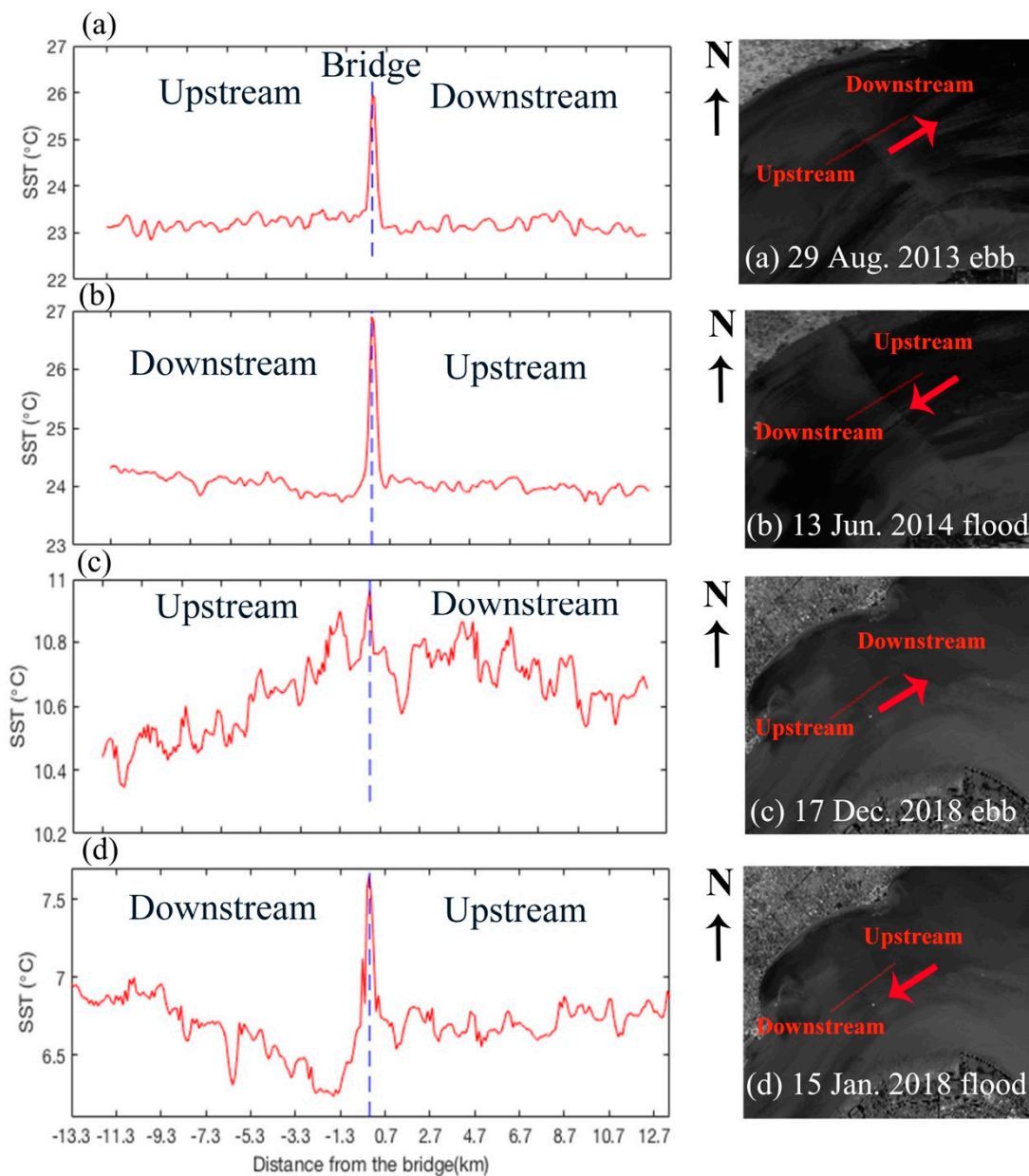


Figure 7. SST along transects obtained from Landsat 8 on 29 August 2013 (a), 13 June 2014 (b), 17 December 2018 (c) and 15 January 2018 (d). Vertical blue dashed line denotes the bridge.

3.4. Increased SSC Downstream of the Bridges

It can be seen that the SSC of Hangzhou Bay is generally high and there is a great difference within the bay (Figure 8). In the middle of Hangzhou Bay, the SSC is the highest. Furthermore, when the current flows westward, there is a large amount of suspended sediment in the central part of the bay; when the current flows eastward, the SSC in the middle is relatively low. Other areas with high SSCs are the west of Hangzhou Bay, the northeast of Hangzhou Bay near the Yangtze River Estuary and the shallow water sandbanks in the south of Hangzhou Bay. Focusing on the waters near the bridge, it can be found that the downstream SSC increases, which is opposite to the trend for SST. When the current flows westward, the downstream SSC increases greatly. However, when the current flows eastward, the SSC increases little, and it increases significantly only southeast of the bridge (Figure 8).

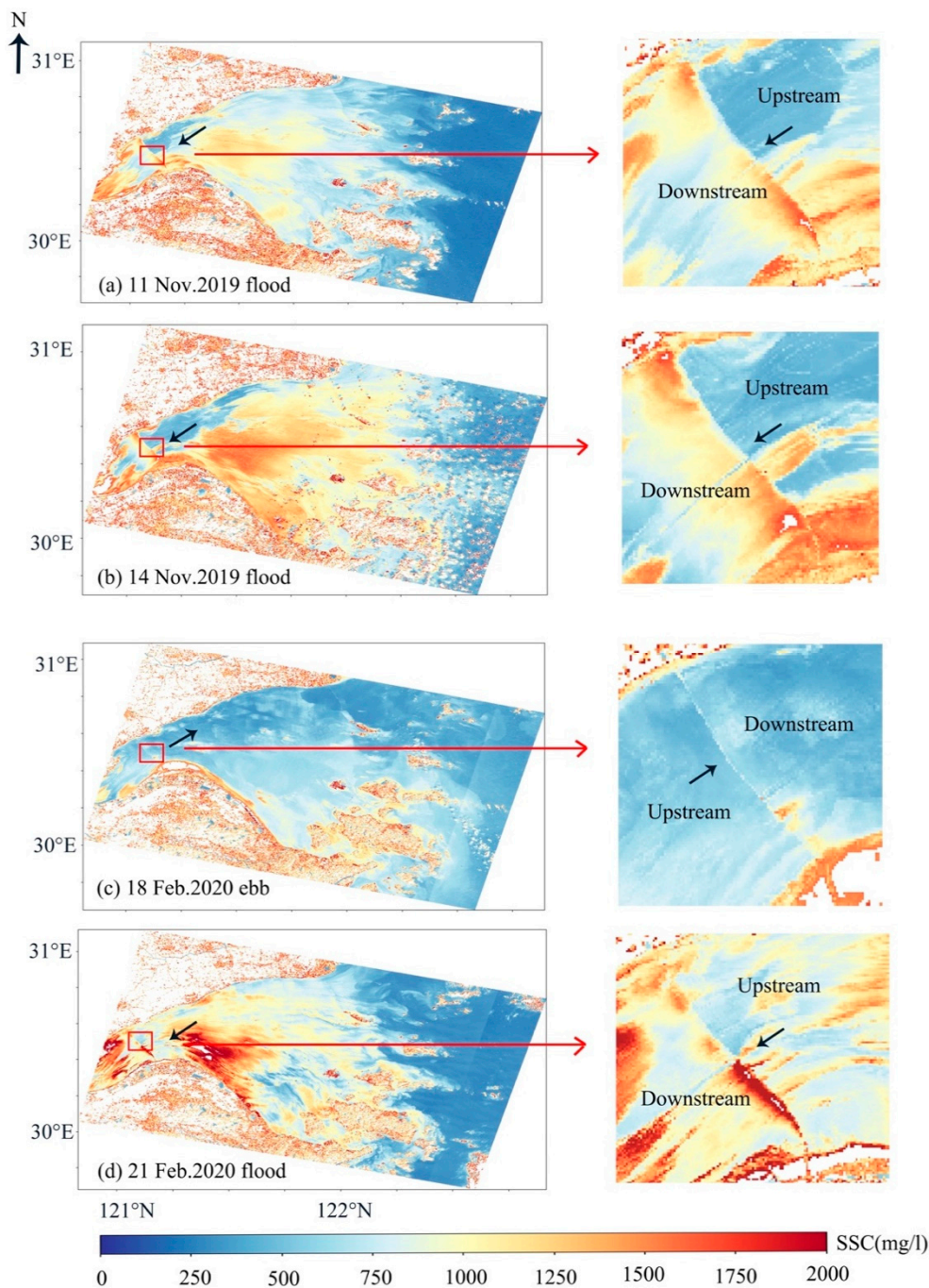


Figure 8. Suspended sediment concentration retrieved from HY-1C data collected on 11 November 2019 (a), 14 November 2019 (b), 18 February 2020 (c) and 21 February 2020 (d). (a,b,d) Flood; (c) ebb.

For each image, we took three transects perpendicular to the bridge to observe the increasing range of SSCs upstream and downstream. It was found that the SSC increases within the range of 0.3–6.0 km downstream (Figure 9) and the closer to the bridge, the greater the SSC value. The maximum value of SSC appears at approximately 0.5–1.0 km downstream. The downstream suspended sediment is mostly concentrated in 0.3–4.0 km, while in the range of 4.0–6.0 km, although the SSC increases, the SSC value is less. The bridge is like a pair of scissors, which divides the upstream and downstream SSCs into two parts. There is a clear dividing line between them, and the bridge is their dividing line. The incremental values of the downstream SSC are 300–1000 mg/L.

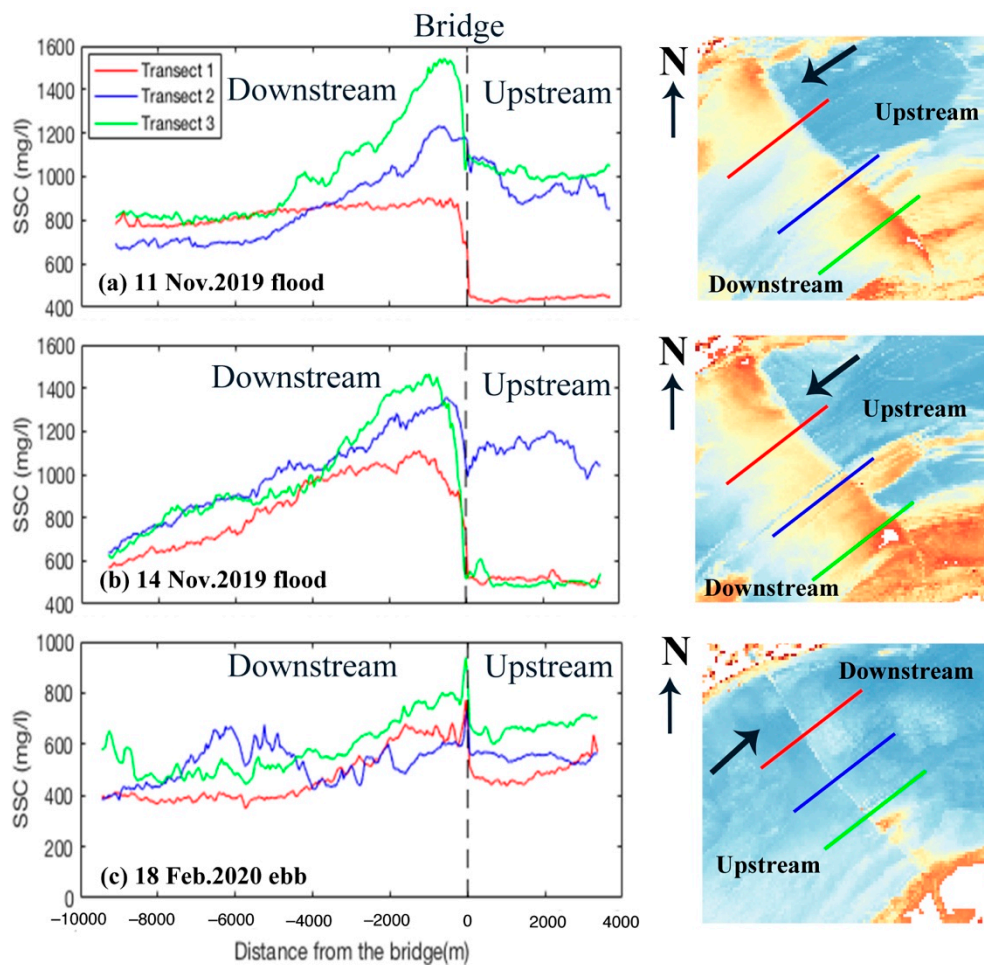


Figure 9. Suspended sediment concentration (SSC along transects obtained from HY-1C on 11 November 2019 (a), 14 November 2019 (b) and 18 February 2020 (c). The vertical black dashed line on the left figure denotes the bridge, and the black arrow pointing to the bridge on the right figure denotes the current direction.

4. Discussion

4.1. Factors Affecting SST Distribution in Hangzhou Bay

The overall distribution of SSTs in Hangzhou Bay is affected by seasonal change [42], tides [43] and currents [44], water injection from the Qiantang and Yangtze Rivers [45], suspended sediment and the Coriolis force [46].

The seasons have an effect on the SST. In winter, the solar radiation is weak, and the winter monsoon, originated from Siberian high pressure, cools the temperature of Hangzhou Bay (Figure 4a,b,e,f,i,j). The SST decreases under the agitation of cold air [47]; in summer, the solar radiation is strong, and the summer monsoon [48], originated from Subtropical high pressure, warms the temperature of Hangzhou Bay, making the SST higher (Figure 4c,d,h).

The distribution of SSTs is affected by tides [43] and currents. The tides strengthen the mixing of the surface water and the bottom water in the vertical direction, and make the deeper cold water surge to the sea surface in the horizontal direction. There is a Taiwan warm current and coastal current in Hangzhou Bay [44]. In winter, under the action of the northerly monsoon, a coastal cold current is generated [49]. It flows to the south and reduces the SST in the north of Hangzhou Bay. At the same time, the northward Taiwan warm current, with high temperature and salinity, cause the SST in the south of Hangzhou Bay to rise (Figure 4a,b,e,f,i,j). These two currents form strong

vertical convection in the northeast of Hangzhou Bay (31° N), and generate upwelling at a steep slope area [44]. Therefore, in the northeast part of Hangzhou Bay near the Yangtze River Estuary, the SST is lower than that in the surrounding waters (Figure 4). In summer, under the action of the southerly monsoon, the northward coastal current is generated, while the Taiwan warm current goes in the same direction [44]. The horizontal and vertical convection is weakened [50], which has no obvious effect on the SST distribution in Hangzhou Bay. Therefore, the SST in the south and north of Hangzhou Bay is evenly distributed in summer (Figure 4c,d,h).

The SST will be influenced by the water injection from the Qiantang and Yangtze Rivers. Every year, the runoff of the Yangtze River carries a lot of fresh water and suspended sediment into the north of Hangzhou Bay [51]. In the northeast of Hangzhou Bay, the concentration of the Yangtze River fresh water is high. In summer, with the large precipitation and the high-temperature rainwater, the Yangtze River carries a lot of warm water into the Hangzhou Bay, increasing the SST of the northeast of Hangzhou Bay near the mouth of the Yangtze river (Figure 4). In winter, the Yangtze River transports a lot of cold water into the north of Hangzhou Bay, decreasing the SST of that water area (Figure 4) [45]. When the Qiantang River is injected from the west of Hangzhou Bay [10], the concentration of fresh water decreases from the top of the bay to the open sea. Just like the runoff of the Yangtze River, it brings a warm water injection in summer, which makes the SST at the top of Hangzhou Bay higher, and conveys a cold water injection in winter, which makes the SST at the top of Hangzhou Bay lower. Therefore, in summer, the SST is higher in the west and lower in the east, while in winter, it is the opposite (Figure 4).

The specific heat capacity of suspended sediment is larger than that of water, and the temperature rises and falls faster [52]. The Qiantang River carries sediment into Hangzhou Bay. Under the action of a tidal bore, there is a high sediment concentration area in the Qiantang River Estuary [53]. Therefore, compared to that of the other waters, the SST of Hangzhou Bay becomes warmer in summer and colder in winter (Figure 4). Reclamation also affects the concentration of suspended sediment [54], which, in turn, changes the SST.

In summer, due to the action of the Coriolis force, the cold seawater in the east is poured into the north of Hangzhou Bay, decreasing the temperature in the north during the rising tide; in the ebb tide, the warm seawater in the west is affected by the Coriolis force, flowing into the south of Hangzhou Bay, increasing the temperature in the south (Figure 4c,d,h), the same as in the winter (Figure 4a,b,e,f,i,j).

4.2. Influence of Cross-Sea Bridge on SST and SSC Distribution

The waters near the Hangzhou Bay Bridge, before the completion of the bridge, had a uniform distribution of SSC [55]. However, after the bridge was built, the bridge piers changed the hydrodynamic environment, inducing the downstream SST to decrease and the downstream SSC to increase. They have a certain gradient characteristic. The bridge is like a pair of scissors, which separates the upstream and downstream SSC tidily, as well as the SST, resulting in an obvious boundary, which divides the SSC (SST) into two obvious parts. The SSC (SST) is no longer evenly distributed (Figures 4 and 8) near the bridge. In other waters without bridges in Hangzhou Bay, the SST and SSC are distributed evenly.

After the completion of the bridge, due to the water-blocking effect of the pier, the flow structure of the upstream current varies. A portion of the flow in front of the pier passes around the pier, forming a vertical vortex on both sides of the pier. The other portion is dispersed into upward and downward directions [56]. The surface water curving upward forms backwater in front of the pier, which makes the upstream water level rise. The lower flow scours the riverbed downward and produces a horseshoe vortex on the riverbed [57]. Therefore, the flow structure around the pier includes the downward flow in front of the pier, the water surge in front of the pier and the large-scale vortex system.

When the water flows through the pier, the cross-section becomes more narrow due to the compression of the pier, and the velocity between the piers raises, generating local flow with high velocity characteristics at the front and side of the pier. The local flow scours the front end of the pier violently. When its velocity is greater than the threshold velocity of riverbed sediment [23],

the sediment around the pier begins to move, shaping a local scour pit [58]. The scour pit expands and deepens until the sediment washed away is balanced with the sediment from upstream. The scouring at the front end of the pier stops; meanwhile, the depth of the scour pit reaches the maximum. However, the scouring behind the pier continues, and the upward flow at the rear of the pier carries the sediment and bottom cold water washed out from the pit downstream [56], which reduces the downstream SST and increases the downstream SSC.

The vortex system includes the horseshoe vortex in front of the pier and the wake vortex downstream of the pier [22,59]. Due to the existence of an unstable shear stress layer, the upstream traveling flow separates on both sides of the pier. Wake vortices are continuously released between the mainstream separation boundary and the pier. Each time a wake vortex is released, a low-pressure center appears. When the wake vortex is carried down by the current, it affects the fluid in the horseshoe-shaped vortex area to make lateral, vertical and back-to-back swings. Like a vacuum cleaner, the sediment and cold water on the bed surface are brought to the downstream sea surface [23], which reduces the downstream SST and increases the downstream SSC. When the Reynolds number is small, the vortex system is stable. However, in practice, the Reynolds number is very large, and the wake vortex is extremely unstable and continuously releases from both sides of the pier [60].

In summer, the SST is relatively high, induced by the higher air temperature, and the temperature difference between surface and depth is large; when the bottom cold water is brought to the sea surface, the change in the downstream SST is more obvious (Figure 5c); in winter, the SST is relatively low, induced by the lower air temperature, and the temperature difference between the surface and depth is small, so there is little change in the downstream SST (Figure 5e,g). The bridge pier spacing of the Hangzhou Bay sea-crossing bridge is mostly between 50 and 90 m, and some piers near the main navigation route are more than 150 m. The backwater area of the piers to the bay reaches 7% [10]. The local scour of 1428 piers reduces the SST in the range of 0.3–4.0 km downstream (Figure 7).

4.3. Comparison of the Influence of the Pier on the SST and SSC

When water flows through the pier, the SST decreases at 0.3–4.0 km downstream, while the SSC increases at 0.3–6.0 km downstream. It is also seen from other literature that the range of influence of the bridge on the downstream SSC is 0.3–6.0 km [10]. The water-blocking effect of the pier changes the upstream flow structure, and wake vortices appear around the pier, which suck the bottom cold water and sediment to the sea surface because of the low-pressure center. From the decreasing range of the SST downstream, it can be inferred that the area of influence of wake vortices on downstream flow is about 0.3–4.0 km. Meanwhile, the wake vortices can also induce higher SSCs within 0.3–4.0 km downstream of the bridge. Additionally, 4.0–6.0 km downstream of the bridge, the SSC is still high due to the currents' transportation [29,61], even with the wake vortices fading away. In a word, within 0.3–4.0 km downstream, the wake vortex causes the SST to decrease and the SSC to increase, while in the range of 4.0–6.0 km downstream, the effect of the wake vortex disappears, and the suspended sediment absorbed continues to be transported by the current, leading to a higher SSC there.

Although the methods used to retrieve the SST and SSC are known, there are still three innovations in this paper. Firstly, the HY-1C satellite, launched in 2018, has novel data, and this paper is the first to use HY-1C data to study the influence of bridges on SSC. Secondly, this is also the first to use satellite data to observe the SST downstream of a bridge and upstream of the bridge to detect the impact of the bridge on the SST of surrounding waters and explore its mechanism. Finally, by comparing the variation ranges of the SST and SSC between upstream and downstream areas, this paper used satellite data for the first time to obtain the mechanism of the influence of a cross-sea bridge on SST and SSC further; that is, the wake vortices around the pier reduce the downstream SST and increase the downstream SSC. If it exceeds the influence range of the wake vortices, the SSC continues to increase due to the current transport, while the SST returns to its original state.

5. Conclusions

The bridge affects the distribution of the SST and SSC in Hangzhou Bay. In general, the downstream SST declines and the downstream SSC increases. The SST decreases in the range of 0.12–0.6 °C and the incremental values of the downstream SSC are 300–1000 mg/L. In summer, when the current flows through the bridge piers, the downstream SST is significantly reduced by a maximum of 3.5%, while in autumn and winter, the downstream SST still declines, but the change is not as obvious as that in summer. The range of influence of the pier on the downstream SST is about 0.3–4.0 km downstream of the bridge, and that for the downstream SSC is 4.0–6.0 km.

After the completion of the bridge, the hydrodynamic environment changed, which affected the SST and SSC distribution in Hangzhou Bay. When the water flows through the pier, the flow structure changes. A portion of the flow is dispersed in upward and downward directions; the downward flow generates local scour. When the scouring at the front end of the pier stops, the upward flow behind the pier brings the sediment and the bottom cold water downstream, causing the downstream SST to decrease and the downstream SSC to increase. The other portion passes around the pier, which generates a wake vortex. Once a wake vortex is released, a low-pressure center appears, sucking the sediment and bottom cold water to the downstream sea surface, decreasing the downstream SST and increasing the downstream SSC (Figure 10).

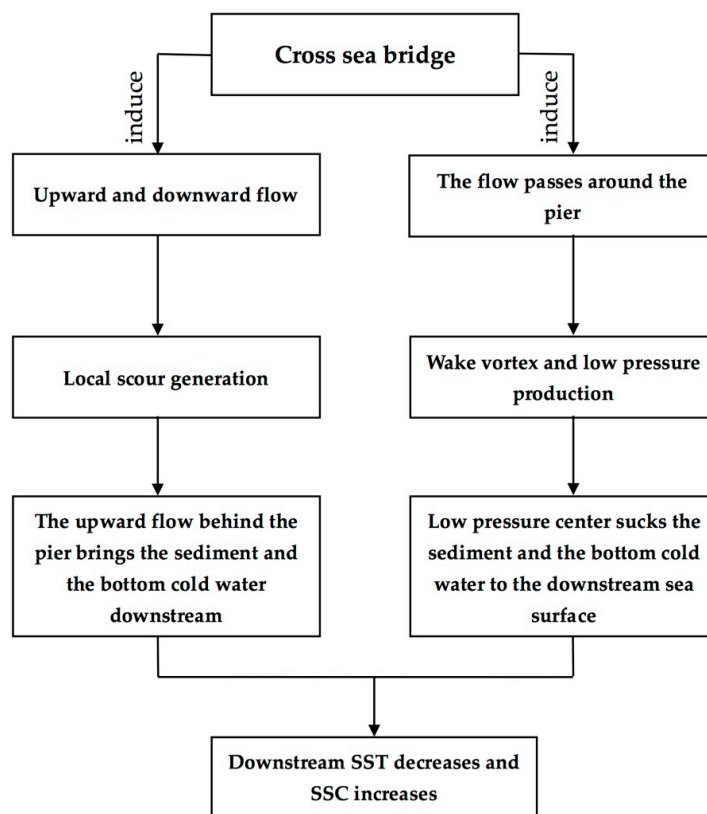


Figure 10. Graphical abstract illustrating how the cross-sea bridge reduces the downstream SST and raises the downstream SSC.

The SSC increases within 0.3–6.0 km downstream, longer than the distance of SST change downstream of the bridge. This is because the wake vortices make a difference to the downstream SST and SSC, with wake vortices' effects occurring over 0.3–4.0 km, leading to a lower SST, higher SSC and no wake-vortex effects within 4.0–6.0 km. Therefore, within the downstream 4.0–6.0 km, there is no cold sea water, while the SSC is still high due to the transport of sediment by currents.

Author Contributions: S.H. and L.C. jointly conducted the research; data collection, processing and analysis; and manuscript writing. J.L. worked on the data collection and data processing and advised the research project. M.Z. performed data processing; J.B. and J.X. performed data collection. All authors have read and agreed to the published version of the manuscript.

Funding: This work was jointly supported by the following research projects: Research Project of Zhejiang Department of Education (Y201840279); Research project of studying on the forecasting systems of the global high resolution marine dynamic environment (2016YFC1401406); Guangdong Key Laboratory of Ocean Remote Sensing (South China Sea Institute of Oceanology Chinese Academy of Sciences) (2017B030301005-LORS2001); The Open Foundation from Marine Sciences in the First-Class Subjects of Zhejiang Province (11104060218); Science and Technology Innovation Activity Plan and New Talent Plan for Zhejiang University Students in 2020 (2020R411007).

Acknowledgments: The data product of HY-1C satellite was obtained from the website <https://osdds.nsoas.org.cn>. The authors wish to thank the National Satellite Ocean Application Service, MNR, of the PRC for the data support. The Center for Earth Observation and Digital Earth, Chinese Academy of Sciences, provided the Landsat 8 data.

Conflicts of Interest: The authors declare no conflict of interest.

References

- Li, P.; Li, G.; Qiao, L.; Chen, X.; Shi, J.; Gao, F.; Wang, N.; Yue, S. Modeling the tidal dynamic changes induced by the bridge in Jiaozhou Bay, Qingdao, China. *Cont. Shelf Res.* **2014**, *84*, 43–53. [[CrossRef](#)]
- Zhao, K.; Qiao, L.; Shi, J.; He, S.; Li, G.; Yin, P. Evolution of sedimentary dynamic environment in the western Jiaozhou Bay, Qingdao, China in the last 30 years. *Estuar. Coast. Shelf Sci.* **2015**, *163*, 244–253. [[CrossRef](#)]
- Qi, J. Modern sedimentation rate and heavy metal accumulation in Jiaozhou Bay sediments. *Science* **2005**, *308*, 1293–1295.
- Qiao, S.; Pan, D.; He, X.; Cui, Q. Numerical Study of the Influence of Donghai Bridge on Sediment Transport in the Mouth of Hangzhou Bay. *Procedia Environ. Sci.* **2011**, *10*, 408–413. [[CrossRef](#)]
- Rasmusson, E.M.; Carpenter, T.H. Variations in tropical sea surface temperature and surface wind fields associated with the Southern Oscillation/El Niño. *Mon. Wea. Rev.* **1982**, *110*, 354–384. [[CrossRef](#)]
- Oka, E.; Kawabe, M. Characteristics of variations of water properties and density structure around the Kuroshio in the East China Sea. *J. Oceanogr.* **1998**, *54*, 605–617. [[CrossRef](#)]
- Sun, Y.; Sun, C.; Wang, X.; Tian, H.; Chen, S. *Forecast of Impact of Qingdao Bay Bridge on Tide, Tidal Current and Residual Current of Jiaozhou Bay: I. Tidal Current of Jiaozhou Bay and Adjacent Sea Area*; Ocean University Qingdao: Qingdao, China, 1994; pp. 105–119.
- Sun, Y.; Tian, H.; Zheng, L.; Chen, S. *Forecast of Impact of Qingdao Bay Bridge on Tide, Tidal Current and Residual Current of Jiaozhou Bay: II. Study of Forecast Method*; Ocean University Qingdao: Qingdao, China, 1994; pp. 120–125.
- Sun, Y.; Wang, X.; Sun, C.; Chen, S. *Forecast of Impact of Qingdao Bay Bridge on Tide, Tidal Current and Residual Current of Jiaozhou Bay: III. Forecast Method and Forecast Results*; Ocean University Qingdao: Qingdao, China, 1994; pp. 126–133.
- Cai, L.; Tang, D.; Levy, G.; Liu, D. Remote sensing of the impacts of construction in coastal waters on suspended particulate matter concentration—The case of the Yangtze River delta, China. *Int. J. Remote Sens.* **2016**, *37*, 2132–2147. [[CrossRef](#)]
- Cai, L.; Zhou, M.; Liu, J.; Tang, D.; Zuo, J. HY-1C Observations of the Impacts of Islands on Suspended Sediment Distribution in Zhoushan Coastal Waters, China. *Remote. Sens.* **2020**, *12*, 1766. [[CrossRef](#)]
- Li, J.; Gao, S.; Wang, Y.P. Delineating suspended sediment concentration patterns in surface waters of the Changjiang Estuary by remote sensing analysis. *Acta Oceanol. Sin.* **2010**, *29*, 38–47. [[CrossRef](#)]
- Hu, Y.; Yu, Z.; Zhou, B.; Li, Y.; Yin, S.; He, X.; Peng, X.; Shum, C. Tidal-driven variation of suspended sediment in Hangzhou Bay based on GOCI data. *Int. J. Appl. Earth Obs. Geoinf.* **2019**, *82*. [[CrossRef](#)]
- Tanimoto, Y.; Nakamura, H.; Kagimoto, T.; Yamane, S. An active role of extratropical sea surface temperature anomalies in determining anomalous turbulent heat flux. *J. Geophys. Res. Space Phys.* **2003**, *108*, 108. [[CrossRef](#)]
- Yeh, S.; Kim, C.-H. Recent warming in the Yellow/East China Sea during winter and the associated atmospheric circulation. *Cont. Shelf Res.* **2010**, *30*, 1428–1434. [[CrossRef](#)]
- Deng, Z.; Xie, L.; Han, G.; Zhang, X.; Wu, K. The effect of Coriolis-Stokes forcing on upper ocean circulation in a two-way coupled wave-current model. *Chin. J. Oceanol. Limnol.* **2012**, *30*, 321–335. [[CrossRef](#)]

17. Jiménez-Muñoz, J.C.; Sobrino, J.A. A generalized single-channel method for retrieving land surface temperature from remote sensing data. *J. Geophys. Res.* **2003**, *108*. [[CrossRef](#)]
18. Qin, Z.; Karnieli, A.; Berliner, P. A mono-window algorithm for retrieving land surface temperature from Landsat TM data and its application to the Israel-Egypt border region. *Int. J. Remote Sens.* **2001**, *22*, 3719–3746. [[CrossRef](#)]
19. Wang, F.; Qin, Z.; Song, C.; Tu, L.; Karnieli, A.; Zhao, S. An Improved Mono-Window Algorithm for Land Surface Temperature Retrieval from Landsat 8 Thermal Infrared Sensor Data. *Remote Sens.* **2015**, *7*, 4268–4289. [[CrossRef](#)]
20. McConaghy, D.C. Measuring sea surface temperature from satellites: A ground truth approach. *Remote Sens. Environ.* **1980**, *10*, 307–310. [[CrossRef](#)]
21. Saldías, G.S.; Lara, C. Satellite-derived sea surface temperature fronts in a river-influenced coastal upwelling area off central-southern Chile. *Reg. Stud. Mar. Sci.* **2020**, *37*, 101322. [[CrossRef](#)]
22. Unger, J.; Hager, W.H. Down-flow and horseshoe vortex characteristics of sediment embedded bridge piers. *Exp. Fluids* **2007**, *42*, 1–19. [[CrossRef](#)]
23. Zhou, Y.; Wang, Y. Forecast of the Bridge Local Scour Depth. *J. Xi'an Highw. Univ.* **1999**, *19*, 48–50.
24. Wang, F.; Zhou, B.; Xu, J.; Song, L.; Wang, X. Application of neural network and MODIS 250 m imagery for estimating suspended sediments concentration in Hangzhou Bay, China. *Environ. Geol.* **2009**, *56*, 1093–1101. [[CrossRef](#)]
25. Liu, C.; Sui, J.; He, Y.; Hirshfield, F. Changes in runoff and sediment load from major Chinese rivers to the Pacific Ocean over the period 1955–2010. *Int. J. Sediment Res.* **2013**, *28*, 486–495. [[CrossRef](#)]
26. Xie, D.; Wang, Z.B.; Gao, S.; De Vriend, H. Modeling the tidal channel morphodynamics in a macro-tidal embayment, Hangzhou Bay, China. *Cont. Shelf Res.* **2009**, *29*, 1757–1767. [[CrossRef](#)]
27. Xie, D.; Gao, S.; Wang, Z.B.; Pan, C.-H. Numerical modeling of tidal currents, sediment transport and morphological evolution in Hangzhou Bay, China. *Int. J. Sediment Res.* **2013**, *28*, 316–328. [[CrossRef](#)]
28. Ni, Y.Q.; Geng, Z.Q.; Zhu, J.Z. Study on characteristic of hydrodynamics in Hangzhou Bay. *J. Hydrodyn.* **2003**, *18*, 439–445.
29. Zhang, Z.; Wu, C.; Huo, Y. The principle of a model SLC9-2 current meter and its handling. *J. Mar. Sci.* **2000**, *1*, 61–64.
30. Wang, S.M.; Wang, Z.; He, Q.Y.; Zhang, J.; Zhang, Y.Q. Structure Design of the ANSYS-Based SLC9-2-Type Direct Reading Current Meter. *Adv. Mater. Res.* **2014**, *926*, 1412–1416. [[CrossRef](#)]
31. Zhu, W.; Pang, S.; Chen, J.; Sun, N.; Huang, L.; Zhang, Y.; Zhang, Z.; He, S.; Cheng, Q. Spatiotemporal variations of total suspended matter in complex archipelagic regions using a sigmoid model and Landsat-8 imagery. *Reg. Stud. Mar. Sci.* **2020**, *36*, 101308. [[CrossRef](#)]
32. Carlson, T.N.; Ripley, D.A. On the relation between NDVI, fractional vegetation cover, and leaf area index. *Remote Sens. Environ.* **1997**, *62*, 241–252. [[CrossRef](#)]
33. Sobrino, J.A.; Raissouni, N. Toward remote sensing methods for land cover dynamic monitoring: Application to Morocco. *Int. J. Remote Sens.* **2000**, *21*, 353–366. [[CrossRef](#)]
34. Sobrino, J.A.; Jiménez-Muñoz, J.C.; Paolini, L. Land surface temperature retrieval from LANDSAT TM 5. *Remote Sens. Environ.* **2004**, *90*, 434–440. [[CrossRef](#)]
35. Sobrino, J.A.; Jimenez-Munoz, J.C.; Soria, G.; Romaguera, M.; Guanter, L.; Moreno, J.; Plaza, J.; Martinez, P.; Jimenez-Muoz, J. Land Surface Emissivity Retrieval from Different VNIR and TIR Sensors. *IEEE Trans. Geosci. Remote. Sens.* **2008**, *46*, 316–327. [[CrossRef](#)]
36. Wen-Yao, L.; Field, R.; Gantt, R.; Klemas, V. Measurement of the surface emissivity of turbid waters. *Remote Sens. Environ.* **1987**, *21*, 97–109. [[CrossRef](#)]
37. Wang, L.; Lu, Y.; Yao, Y. Comparison of Three Algorithms for the Retrieval of Land Surface Temperature from Landsat 8 Images. *Sensors* **2019**, *19*, 5049. [[CrossRef](#)]
38. Nikam, B.R.; Ibragimov, F.; Chouksey, A.; Garg, V.; Aggarwal, S.P. Retrieval of land surface temperature from Landsat 8 TIRS for the command area of Mula irrigation project. *Environ. Earth Sci.* **2016**, *75*, 1169. [[CrossRef](#)]
39. Hadjimitsis, D.G.; Hadjimitsis, M.G.; Clayton, C.R.I.; Clarke, B.A. Determination of Turbidity in Kourris Dam in Cyprus Utilizing Landsat TM Remotely Sensed Data. *Water Resour. Manag.* **2006**, *20*, 449–465. [[CrossRef](#)]
40. Lenoble, J.; Herman, M. Radiative transfer in the Earth's atmosphere. *Aerosol Remote Sens.* **2013**, 53–86. [[CrossRef](#)]

41. Chen, X.-Y.; Zhang, J.; Tong, C.; Liu, R.-J.; Mu, B.; Ding, J. Retrieval Algorithm of Chlorophyll-a Concentration in Turbid Waters from Satellite HY-1C Coastal Zone Imager Data. *J. Coast. Res.* **2019**, *90*, 146–155. [[CrossRef](#)]
42. Cho, Y.-K.; Lee, K.-S.; Park, K.-Y. Year-to-year Variability of the Vertical Temperature Structure in the Youngsan Estuary. *Ocean Polar Res.* **2009**, *31*, 239–246. [[CrossRef](#)]
43. Padilla, E.M.; Díez-Minguito, M.; Sánchez, M.O.; Losada, M.A. A Subtidal Model of Temperature for a Well-Mixed Narrow Estuary: The Guadalquivir River Estuary (SW Spain). *Chesap. Sci.* **2015**, *39*, 605–620. [[CrossRef](#)]
44. Liu, X.-Q.; Yin, B.-S.; Hou, Y.-J. The dynamic of circulation and temperature-salinity structure in the changjiang mouth and its adjacent marine area II. Major characteristics of the circulation. *Oceanol. Limnol. Sin.* **2008**, *39*, 312–320.
45. Zhou, X.-Y.; Hu, D.-B.; Wang, C.-Z.; Hu, X.-J.; Yao, S.-K. Seasonal and Interannual SST Variations in the Changjiang Estuary. *J. Ocean Univ. Qingdao* **2005**, *35*, 357–362.
46. Li, S.; Sun, W. Numerical Modeling of Residual Currents in Hangzhou Bay. *Oceanol. Limnol. Sin.* **1995**, *26*, 254–261.
47. Wang, Q.; Li, Z. Numerical simulation of water temperature under diurnal variation of air temperature in the Hangzhou Bay. *Mar. Sci. Bull.* **2018**, *37*, 303–309.
48. Zhu, Q.; He, J.; Wang, P. A study of circulation differences between East-Asian and Indian summer monsoons with their interaction. *Adv. Atmos. Sci.* **1986**, *3*, 466–477.
49. Zou, T.; Gao, H.-W.; Sun, W.-X.; Liu, Z. Numerical Simulation of Lagrange Residual Current in the Changjiang Estuary, Hangzhou Bay and Their Adjacent Sea I: Barotropic Circulation. *Period. Ocean Univ. China* **2009**, *39*, 153–159.
50. Liu, X.-Q.; Hou, Y.-J.; Yin, B.-S.; Yang, D.-Z. Dynamics of circulation and temperature-salinity structures in changjiang river mouth and its adjacent sea III. The temperature structure. *Oceanol. Limnol. Sin.* **2015**, *46*, 526–533.
51. Liu, X.; Lu, Y.; Pan, L. Tidal current numerical simulating and water exchange research in Yangtze Estuary and Hangzhou Bay. *J. Hydrodyn.* **2006**, *21*, 171–180.
52. Zhang, F.; Wu, T. Sediment concentration measurement based on thermal capacity. *J. Hohai Univ. (Nat. Sci.)* **2013**, *41*, 456–460.
53. Pan, C.; Huang, W. Numerical Modeling of Suspended Sediment Transport Affected by Tidal Bore in Qiantang Estuary. *J. Coast. Res.* **2010**, *26*, 1123–1132. [[CrossRef](#)]
54. Li, L.; Taoyan, Y.; Lu, Z.; Yanming, Y.; Yuezhang, X. Influences of reclamation location on the water and sediment environment in Hangzhou Bay. *J. Harbin Eng. Univ.* **2019**, *40*, 1870–1875.
55. Chen, X. The Analysis of Multitemporal Remote Sensing Images for Suspended Sediment in Hangzhou Bay. *J. Remote Sens.* **1989**, 128–135.
56. Zhang, X.-Y.; Lv, H.-X.; Shen, B. Experimental studies on local scour mechanism of cylinder bridge piers. *Hydro Sci. Eng.* **2012**, *2*, 34–41.
57. Qi, M.-L. Riverbed scouring around bridge piers in river section with sand pits. *J. Hydraul. Eng.* **2005**, *7*, 835–839.
58. Olsen, N.R.B.; Kjellesvig, H.M. Three-dimensional numerical flow modeling for estimation of maximum local scour depth. *J. Hydraul. Res.* **1998**, *36*, 579–590. [[CrossRef](#)]
59. Pasiok, R.; Stilger-Szydło, E. Sediment particles and turbulent flow simulation around bridge piers. *Arch. Civ. Mech. Eng.* **2010**, *10*, 67–79. [[CrossRef](#)]
60. Roulund, A.; Sumer, B.M.; Fredsøe, J.; Michelsen, J. Numerical and experimental investigation of flow and scour around a circular pile. *J. Fluid Mech.* **2005**, *534*, 351–401. [[CrossRef](#)]
61. Su, J.; Wang, K.; Li, Y. Fronts and transport of suspended matter in the Hangzhou Bay. *Acta Oceanol. Sin.* **1993**, *12*, 1–15.

